IEEE Access
Multidisciplinary | Rapid Review | Open Access Journal

Received April 28, 2019, accepted June 27, 2019, date of publication July 5, 2019, date of current version August 2, 2019.

Digital Object Identifier 10.1109/ACCESS.2019.2926793

Design and Control of Field-Free Region Using Two Permanent Magnets for Selective Magnetic Hyperthermia

ARMANDO RAMOS SEBASTIAN[1], SE HWAN RYU[2], HAYE MIN KO[2], AND SUNG HOON KIM[1], (Member, IEEE)

[1]Department of Electronics Convergence Engineering, Wonkwang University, Iksan 54538, South Korea
[2]Department of Bio-Nano Chemistry, Wonkwang University, Iksan 54538, South Korea

Corresponding authors: Haye Min Ko (hayeminko@wku.ac.kr) and Sung Hoon Kim (kshoon@wku.ac.kr)

This work was supported by the Basic Science Research Program through the National Research Foundation of Korea (NRF), funded by the Ministry of Education, the Ministry of Science, ICT and Future Planning under Grant NRF-2015R1D1A1A01057463, Grant 2018R1C1B6003491, Grant 2018R1D1A1B07042179, and Grant 2017R1A4A1015594.

ABSTRACT Magnetic hyperthermia using magnetic nano particles (MNPs) is a very innovative method for application in cancer therapy. However, the heat generated by MNPs can destroy normal cells, which necessitates localized heat treatment methods to minimize the damage inflicted by magnetic hyperthermia. One such method involves the use of a field-free region (FFR). In this paper, the conditions for controlling the FFR based on the magnetic properties of the MNPs were theoretically calculated and verified through experiments. The strength of the gradient magnetic field for controlling the FFR was determined by the relationship between the nanoparticle size, the magnetizing condition, and the temperature change depending on the strength of the AMF. Based on this, a new method for the quantitative generation and control of FFR for selective heat treatment was proposed. We tested the selective heating and temperature control by controlling the FFR. We observed the changing dimension of FFR and heat distribution of MNPs according to changes in the gradient field. When we used 9.56 nm sized MNPs and controlled the distance between two magnets, the area of FFR varied from a minimum of 7.41 cm^2 to a maximum of 26.24 cm^2. In addition, the temperature increase varied from approximately 5 to 45 K when the FFR was controlled using an AMF operating at 12 kA/m and 207 kHz. We hope our findings will be a crucial consideration in system design and potentially in effective cancer therapy.

INDEX TERMS Selective hyperthermia, field-free region (FFR), Fe_3O_4MNPs, superparamagnetic theory.

I. INTRODUCTION

Magnetic hyperthermia is a promising technique for cancer therapy: it induces apoptosis or necrosis of cancerous cells using the heat that magnetic nanoparticles (MNPs) produce when exposed to an alternating magnetic field (AMF) with a typical frequency of hundreds of kilohertz [1]. The ability to focus heating only where nanoparticles are located has drawn the attention of many researchers, up to the point that a clinical system has been developed and its use has been approved in Europe [2]. Its viability has been clinically proven by subjecting patients in patients with prostate and brain cancer to magnetic hyperthermia [3], [4]. Despite its promising results, the optimization of the maximum allowable magnetic field conditions and development of an efficient targeting method remain elusive, owing to which its clinical use has not been extended outside Europe [5]. AMF induce eddy currents within the body, and if they are sufficiently high, they can lead to undesired heating and can damage healthy tissues. To avoid this, Atkinson et al. suggested that the product of the frequency and amplitude of the AMF must be below $4.85 \times 10^8 A/m \cdot s$ [6]. This limit, known as the Atkinson-Brezovich limit, has been used as a reference in several studies; however, the actual maximum parameters for AMF vary for different tissues [7]. Several methods have been developed for administrating MNPs into the area to be treated. Nanoparticles might be injected directly into the tumor: 76-97% of the MNPs supplied by this method [8]. They can

The associate editor coordinating the review of this manuscript and approving it for publication was Rajeswari Sundararajan.

also be administered to the bloodstream and be passively targeted to cancerous cells utilizing the physical properties of the nanoparticles, such as their core size or their hydrophilic or hydrophobic nature [9]–[10]. Additionally, active targeting can be achieved by functionalization of the nanoparticles with ligands such as antibodies for tumorous cells or encapsulation within liposomes or micelles [11], [12]. Sangnier *et al.* developed RGD-tagged magnetosomes observing up to an eight-fold increase in the targeting of magnetic particles compared with other similar targeting methods. Although they reported that photothermia is more efficient than magnetic hyperthermia. This is because magnetic hyperthermia is safer and easier to apply owing to its ability to penetrate the tissue, whereas the application of photothermia is mostly limited to superficial tissues [13].

Another approach for active targeting involves dragging MNPs by applying a gradient magnetic field [14]. However, despite the administration method, a huge amount of up to 80–90% of the nanoparticles end up being transported by blood circulation from the targeted area to the liver and the spleen, especially when passive targeting is used [15]. Even though Kettering *et al.* reported a high retention of nanoparticles at the tumor, results were different among the mice and up to 25% of the nanoparticles were found in the liver during the autopsy [8]. The accumulation of MNPs in such organs lead to undesired heating of healthy tissue when exposing the whole body to an AMF, which—if not taken into consideration— can damage healthy organs. Kut et al. intravenously injected mice with different concentrations of dextran-coated MNPs [16]. Six days after the injection, the mice were exposed to an AMF, and high concentrations of nanoparticles were detected in the mice livers and a high mortality rate was observed for the mice treated with a high dose of nanoparticles. It was therefore concluded that the amount of MNPs used should be limited to avoid harm to the healthy tissues, which also hinders magnetic hyperthermia from achieving its maximum efficiency.

Magnetic hyperthermia has been studied in magnetic resonance imaging (MRI) systems, usually by adding a coil for generating the AMF. In such studies, it has been noted that the permanent magnet of the MRI system can saturate the MNPs, impeding them to align with the AMF and reducing the released heat significantly, making it viable only for nanoparticles with small cores [17], [18]. In a different work, a pair of coils, each of which had independent control of the current, was used to produce a static magnetic field, and it was observed that the higher the static magnetic field is, the lower is the temperature achieved by the MNPs [19]. These results show that the application of an additional magnetic field can reduce or suppress the heating properties of MNPs. Because the amount of heat generated depends on the distribution and quantity of MNPs applied to the tumors, Gooneratne *et al.* designed a giant magnetoresistance probe to measure such parameters that could predict the location and characteristics of the AMF to be applied during therapy. However, it is difficult to apply this approach effectively at any part of the body owing to its invasive nature [20]. Magnetic particle imaging (MPI) is a non-invasive imaging method first developed by Gleich and Weizenecker based on the nonlinear magnetization of MNPs [21]. As developed by Weizenecker *et al.* a typical MPI system consists of at least one excitation coil used to magnetize the MNPs with an AMF and a receiving coil to measure their magnetization [22]. In order to confine the response of MNPs to a small area, a static magnetic field comprising a field-Free region (FFR) in the center and linearly increasing magnetic field radiating in all directions outward is applied, usually using a pair of magnets with opposing poles facing each other. This field saturates all the MNPs found outside the FFR, impeding them to align with the AMF. Finally, to move the FFR through the working space, an offset is applied, usually by using Helmholtz coils. Compared to other imaging methods, such as computed tomography scan, MPI offers advantages such as the use of non-ionizing radiation, absence of background signals, and a high resolution. For these reasons, MPI has been thoroughly investigated, leading to a wide scope for its applications, such as in the monitoring of stem cells for targeted applications and the development of real- time catheter tracking [23], [24]. Furthermore, systems that can steer MNPs while simultaneously performing MPI have been developed, leading to the design of a system for 3D real-time tracking and steering of a catheter using multi-color MPI [25], [26]. Although MNPs are not distributed uniformly within the tumors, by using the above described systems, MNPs can be distributed evenly in the targeted region. Because the physics related to MPI is quite similar to the principle behind magnetic hyperthermia, Murase et all. investigated the applicability of MPI results in magnetic hyperthermia and found that images obtained by MPI can be used to predict the therapeutic effect of magnetic hyperthermia [27]. Going a step further, Hensley *et al.* proposed using the principle of the FFR to focus the heating in magnetic hyperthermia to any desired area and developed a system capable of performing MPI and selective magnetic hyperthermia [28]. In such system, a pair of magnets is used to create the FFR and the desired targeted region is moved by linear stages and motors to the FFR. Ho *et al.* proposed the use of an FFR to focus the heating and controlled its size by using a set of six DC coils [29]. Tasci *et al.* also proposed using the FFR approach to control the heating of MNPs by using a pair of DC solenoids to create a gradient magnetic field [30]. They showed how the application of the FFR reduced the increase in temperature in MNPs injected in the tails of several rats through in vivo experiments. However, these studies do not consider the magnetic properties of the MNPs, making it impossible to know if the system can be used with any given sample of MNPS. Although there have been reported examples of using a FFR in heat generation, a generalized method has not been reported with defined control conditions and temperature control methods for establishing a FFR according to the size and magnetization characteristics of MNPs.

In this paper, we propose a method to quantitatively control the FFR according to the size and magnetization state of MNPs. Magnetization curves were obtained theoretically according to the size of the MNPs and the strength of the magnetic field for FFR generation was determined. The generated area of FFR was predicted by the simulation according to changes in the field gradient and verified through thermal distribution experiments involving the MNPs. For experimental verification, the strength of the external magnetic field for controlling the 9.56-nm-sized MNPs was calculated theoretically. Although MNPs with larger core sizes exhibit a higher specific absorption rate, and hence higher heating performance, nanoparticles with an approximate size of 10nm were chosen owing to their superparamagnetic properties which are desirable for this selective magnetic hyperthermia approach. By using two permanent magnets that can satisfy the calculated field strength, a FFR was generated and the gap between the magnets was adjusted to generate a gradient magnetic field corresponding to the theoretical value, and heat distribution of the nanoparticles was observed while adjusting the dimension of the FFR. Using an AMF at 12 kA/m and 207 kHz, the temperature was increased in the MNPs and the temperature change was observed using a thermal image camera.

II. HEATING MECHANISM FOR SELECTIVE HYPERTHERIMA

A. PREPARING Fe_3O_4 MNPs

Commercial available iron (II) chloride tetrahydrate ($FeCl_2{\cdot}4H_2O$) and iron (III) chloride hexahydrate ($FeCl_3{\cdot}6H_2O$) were provided by Wako chemicals. Sodium hydroxide was purchased from Samchun Chemicals. All the chemicals were used without further purification. Water was distilled by a Q-Grad 1 purification cartridge from Millipore water purification systems to obtain ultrapure water. Following the general procedure, iron (II) chloride tetrahydrate (2.65 g, 13.32 mmol) and iron (III) chloride hexahydrate (7.208 g, 26.66 mmol) were dissolved in ultrapure water (160 ml) in air. After vigorous stirring at room temperature for 10 min, sodium hydroxide (NaOH, 9.6 g, 0.24 mol) in ultrapure water (40 mL) was added dropwise over 5 min, which immediately led to the formation of a black precipitate, and the reaction mixture was stirred for 30 min to complete the reaction. This black precipitate was separated by filtration using a Buchner funnel and washed repeatedly with ultrapure water until a neutral pH of 7 was obtained. The iron oxide nanoparticles were dried in an oven at 50 °C for 21 h, and the residual water was concentrated under reduced pressure at 70 °C for 21 h. We thus fabricated Fe_3O_4MNPs. Through XRD and VSM, we observed the X-ray diffraction pattern for the fabricated MNPs and the magnetic properties, as shown in Fig. 1. The MNPs showed the six diffraction peaks of the Fe_3O_4 crystal with a cubic spinel structure. The average size of the MNPs was approximately 9.56 nm, as calculated by XRD analysis. The fabricated MNPs represented a

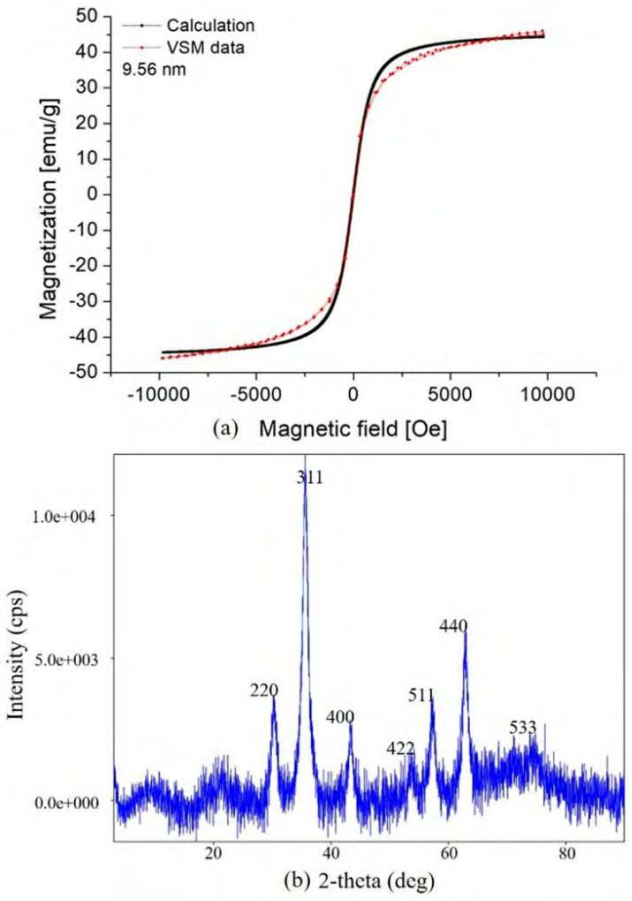

FIGURE 1. (a) Magnetization curves: Comparison of calculation and experimental results and (b) XRD analysis of the fabricated Fe_3O_4.

magnetization of 47.622 emu/g and a coercive force of 8.92 Oe. The black line shows the measured data, whereas the red line represents the results calculated for MNPs with a size of 9.56 nm using Langevin's theory.

B. PRINCIPLE OF FIELD-FREE REGION (FFR)

Unlike multidomain magnetic nanoparticles that produce heat by a combination of hysteresis losses and magnetic relaxation, the heating mechanism for magnetic hyperthermia in single domain MNPs is limited to both Neel and Brownian motions in an AMF. The restriction of the two motions can control the increase in the heat of the Fe_3O_4 MNPs. Therefore, a static magnetic field (SMF) can be used to limit the two motions of the Fe_3O_4 MNPs. For selective hyperthermia, a field-free region (FFR) is generated in the environment of SMF. The SMF restricts the heat generation of Fe_3O_4 MNPs, whereas an FFR inside the SMF allows heat generation by them. To establish the FFR, we utilized two permanent magnets. When the two magnets face the same pole, the gradient field and FFR are created, as shown in Fig. 2. The distance between the two magnets determines the strength of the gradient field and the dimension of the FFR.

When MNPs are saturated, the strength of the magnetic field is different owing to changes in the size of the MNPs.

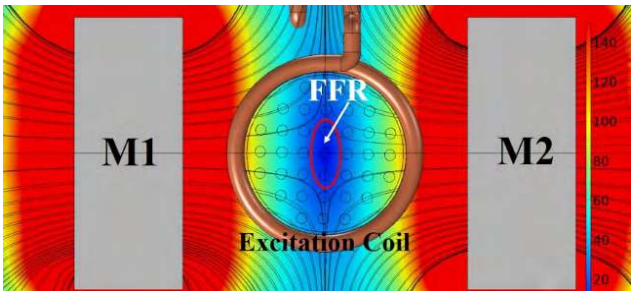

FIGURE 2. A method to generate a field-free region using two permanent magnets.

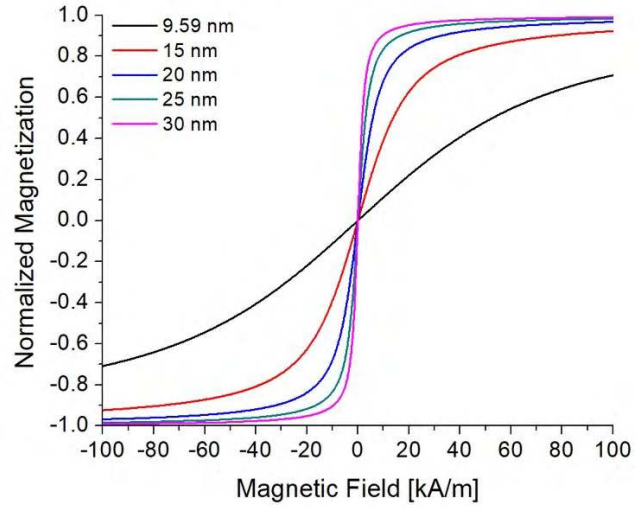

FIGURE 3. Magnetization curves calculated using Langevin's theory according to changes in the size of MNPs.

Langevin's theory of paramagnetism is used, because of its simplicity and the good approximation of real values it offers without restoring to more complex models. According to the theory, the magnetization of a given concentration of MNPs can be expressed as follows [31]:

$$\boldsymbol{M}(\boldsymbol{H}, t) = n\boldsymbol{m}\mathcal{L}(\alpha) \tag{1}$$

where n is the iron concentration in the particles, $\boldsymbol{m}$ the magnetic moment of each particle and $\mathcal{L}(\alpha)$ is the Langevin function, defined as follows:

$$\mathcal{L}(\alpha) = \left(\boldsymbol{coth\alpha} - \frac{1}{\alpha}\right) \tag{2}$$

wherein $\alpha = \mu_0 \boldsymbol{mH}/k_B T_p$.

Here, μ_0 is the vacuum magnetic permeability, $\boldsymbol{H}$ the magnetic field strength, k_B is the Boltzmann's constant and T_p is the temperature of the particles in the Kelvins.

Using Eq. (1), magnetization curves were obtained MNP sizes of up to 30 nm, as shown in Fig. 3. The larger the size of the MNPs is, the lower is the magnetic field required to reach saturation on the magnetization curves. Using the magnetization curves, we investigated the Hs, or the external magnetic fields, required to reach 80% of the saturation magnetization, as shown in TABLE 1. The size of 9.59 nm is required at a static field of 146.49 kA/m to reach the Hs

TABLE 1. Variation in magnetic properties according to core size.

Core Diameter Size (nm)	Hs [kA m^{-1}] at 80%
9.59	146.49
15	38.28
20	16.15
25	8.27
30	4.79

of saturation magnetization. This result fairly consistent with the VSM data, as shown in Fig. 1 (b). MNPs with sizes of 15, 20, and 25 nm attained the Hs at relatively low magnetic fields of 38.28, 16.15, and 8.27 kA/m, respectively. In other words, larger MNPs can relatively easily restrict the Neel and Brownian motions owing to the external magnetic field, because the magnetization value of MNPs becomes larger and thus the temperature rise of MNPs is limited.

In addition, the condition of magnetization is also determined by the external magnetic field. Therefore, when designing MNP-based heat generation systems, the size of the MNPs and the strength of the external magnetic field should be considered together. We adjusted the distance between two permanent magnets to control the dimension of the FFR and the field gradient between the two magnets. At this time, when MNPs are located inside the FFR in the AMF environment, heat is generated, and MNPs located outside the FFR range offer limited heat generation due to the field gradient. In the following part of the study, through simulation and various experiments, we verified and proposed the design and control methods for selective hyperthermia system, as described in Section III

III. EXPERIMENTAL ANALYSIS AND DISCUSSION

Through various experimental analyses, we investigated the performance of heat generation of MNPs for selective hyperthermia. Figure 4 shows the experimental apparatus.

The system consists of an excitation coil to generate the AMF and two permanent magnets to generate the FFR. MNPs (0.035 g) were placed in 13 tubes and were located inside the excitation coil with a diameter of 6 cm. The spacing of each tube was 4 mm and the tube diameter was 8 mm, as shown in Fig. 4 (a). The utilized permanent magnets were of $4cm \times 4cm \times 10cm$ in size and their remanence flux density was 1170 mT. M represents the direction of magnetization. The distance between the two magnets was manually adjusted to 12, 14, and 18 cm when establishing the FFR. Figure 4 (b) shows the strength of the magnetic field of the two magnets within the working space. For these distances, the center of the excitation coil formed the FFR and their gradients were 3.53, 2.33, and 1.11 mT/mm, respectively. Under these conditions, we investigated the dimensions of the FFR, heat

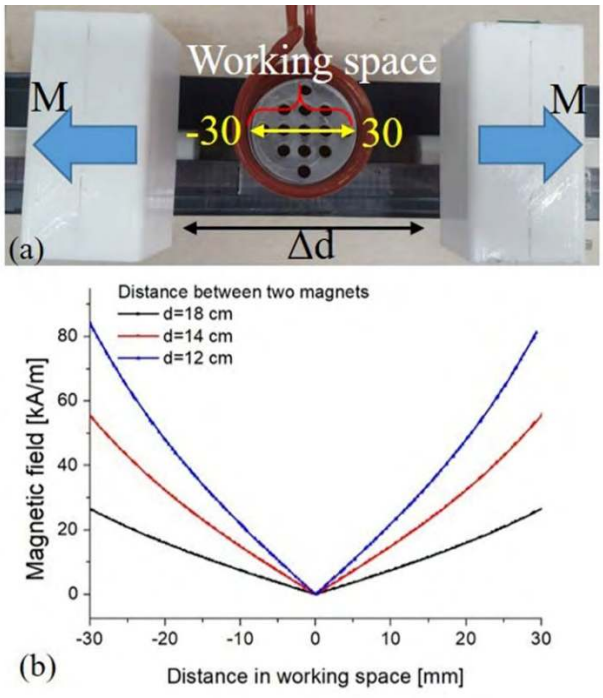

FIGURE 4. (a) Experimental apparatus: It consists of two permanent magnets and, an excitation coil to generate an alternating magnetic field (AMF), and MNPs in 13 containers. (b) Strengths of the magnetic field according to changes in the distance between the two magnets.

generation of MNPs, and selective heat generation through simulation with experiments. First, we investigated the basic temperature of the fabricated MNPs (9.59 nm) for a period of 600 s investigate changes in their values with the applied AMF without a gradient field, as shown in Fig. 5 (a). The applied AMFs of 9.4 (210 kHz), 12 (207kHz), 15.6 (205kHz), and 22 kA/m (204kHz) showed temperature increases of approximately 29, 44.3, 63.5, and 87.7 K, respectively. Thus, the applied AMFs could provide a dynamic range for the temperature rise and were proportional to the increase in temperature.

An external static magnetic field or gradient field is required to ensure that the temperature rise falls within the dynamic range. The range of the temperature rise was adjusted with changes in the strength of magnetic field, as shown in Fig. 5 (b). The applied static field was inversely proportional to the increase in temperature. In this part of the analysis, we considered an external static field of up to 64 kA/m. A higher strength of the AMF led to a wider range of temperature rise. However, a relatively strong SMF is required to reduce the said range. When AMFs of 22 and 15.6 kA/m were applied to the MNPs (9.56 nm) with a SMF of 10 kA/m, the temperature increases were approximately 60 K and 38 K, respectively. To reduce the temperature rise to 20 K, the SMFs of 45 kA/m and 25kA/m were required, respectively. The strengths of SMF are equivalent to the applied magnetic field in a magnetization curve.

The data displayed by the magnetization curves are essential because the SMFs at which the magnetization values

TABLE 2. Relationship between SMF, temperature increase, and Ms %.

SMF (kA m^{-1})	Temperature Increase (K)	Magnetization Saturation (Ms)%
0	44.58	0.000
4	38.19	4.53
8	29.15	9.03
16	19.68	17.79
32	8.18	33.71
64	2.94	56.67

reach the saturation point depend on the size of the MNPs. Larger MNPs require a weaker external magnetic field to reach magnetization saturation (see Fig. 5(b)). The applied SMF can limit or control the temperature rise by limiting the Neel and Brownian motions. When the strength of SMF was zero, the temperature increase was 44.3 K, whereas when it was 28 kA/m at the AMF of 12 kA/m, the temperature increase was 10 K.

We set 10 K as the reference point for the heat control since a person's body temperature is usually 36.5 °C and a temperature rise of 10 K can generate 46.5 °C of heat. In general, it is possible to kill cancer cells at temperature above 42 °C. To attain the temperature increase of 10 K at AMFs of 15.6, 18.7, and 22 kA/m, the SMF needs to be at least 45 kA/m, whereas the AMFs of 9.6 and 12kA/m require relatively low SMFs of 16 and 28 kA/m, respectively. To reach 10K at the AMF of 12 kA/m, the SMF needs to be at 28 kA/m, which corresponds to a magnetization value of 30% of the saturation point in the magnetization curve. If we use smaller MNPs, we can obtain the same temperature increase rate with a weaker SMF based on the magnetization value of 30%.

TABLE 2 shows the magnetization states and temperature increase corresponding to SMF changes at the AMF of 12 kA/m. When the SMF is 64 kA/m, the magnetization curve shows a magnetization value of 56.57 % of the saturation point. In this case, the rate of temperature increase is 2.94 K, and a temperature rise hardly occurs. Through experimental analysis, we found that the strength of SMF required for reaching more than 50% of the MNP saturation point can limit the heat generation of the MNPs. We can use this information to determine the design elements of FFR for selective heat generation and temperature control of MNPs.

The experiments of selective heat generation using FFR were performed for a period of 600 s at the AMF of 12 kA/m with 207 kHz and thermal images were taken at 600 s. We observed the heat generation and heat distribution of MNPs in the 13 tubes without the gradient fields. All MNPs

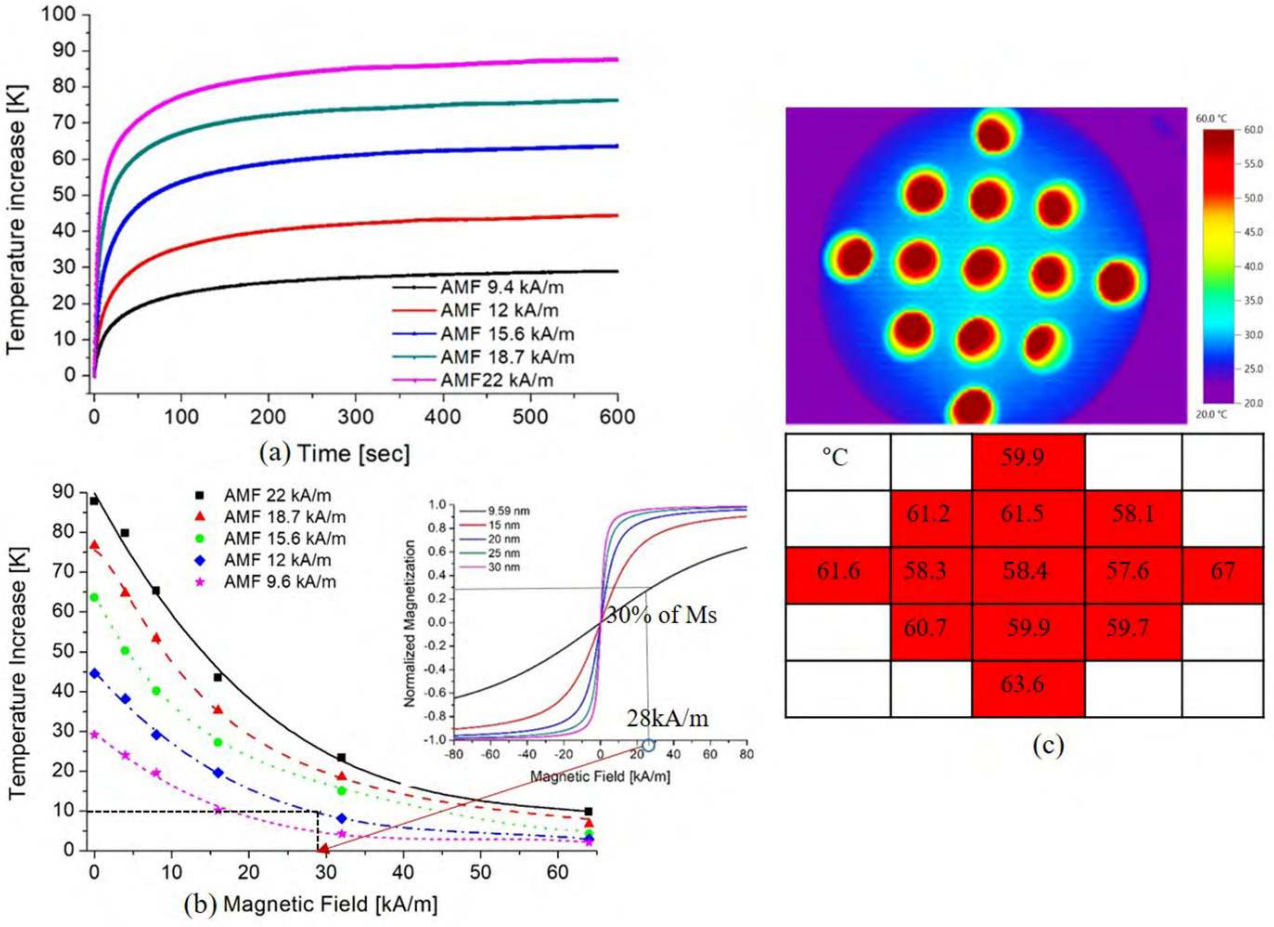

FIGURE 5. (a) Results of temperature increase of MNPs according to changes in the strength of AMF without an applied static magnetic field (SMF). (b) Relationship between the temperature increase and SMF according to changes in AMF. (c) Heat distribution observed using a thermal image camera.

generated heat and the mean value of the maximum temperature in 13 tubes was 60.57 °C, as shown in Fig. 5 (c). The starting temperature for the observations was approximately 16.5 °C. In this case, we could not control the temperature rise because of the FFR.

In the following experiment, we investigated the generation and control of size of the FFR under the applied gradient magnetic fields of 3.53, 2.33, and 1.11 mT/mm using the two permanent magnets. We observed the heat generation with the heat distribution in the 13 tubes under the three conditions, as shown in Fig. 6. When the distance between the two permanent magnets was 18 cm, the generated gradient was 1.11mT/mm and the calculated FFR was 18.91 cm^2 according to magnetic simulation, as shown in Fig. 6 (a1) and (a2). Under the conditions, the FFR distribution was relatively wide, and the distribution of FFR in the simulation was confirmed to be similar to the heat distribution in experiment results, as shown in Fig. 6 (a3). The generated gradient magnetic field was stronger from the center to the magnets, and the gradient magnetic field restricted Neel and Brownian motions. Since the FFR occurred in an elliptical shape, heat generation was highest in the direction from the center to the y-axis, whereas in the x-axis, farther away from the center, the heat generation was lower because of the stronger magnetic field, as shown in Fig. 6 (a3). The heating temperatures at x1, x2, and x3 were 35.5, 44.2, and 51.2 °C, respectively. The temperature distribution from position y1 to position y5 was similar at an average value of 51.74 °C. When the two magnets were closer, at 14 cm apart, the resulting gradient was 2.33 mT/mm. At the working space with a diameter of 6 cm, the maximum magnetic field at the points of ±30 mm was 55 kA/m. In this case, the area of FFR was 7.79 cm^2 as confirmed by simulation and shown in Fig 6 (b1) and (b2). The increase in the gradient reduced the area of the FFR and relatively centralized the heat generation, as shown in Fig. 6 (b3). In other words, the heat generation decreased except at the center because of the increased gradient field. Furthermore, the distribution of FFR and the experimental results were similar. At the center, the temperature was 52.1 °C, whereas the positions x1 and x2 showed temperatures of 26.9 and 36.7 °C, respectively. In the case of the positions y1 and y2, the temperatures were recorded as 43.2 and 47.9 °C, respectively, and the FFR was centered, as shown in Fig. 6 (b3). The accuracy of the

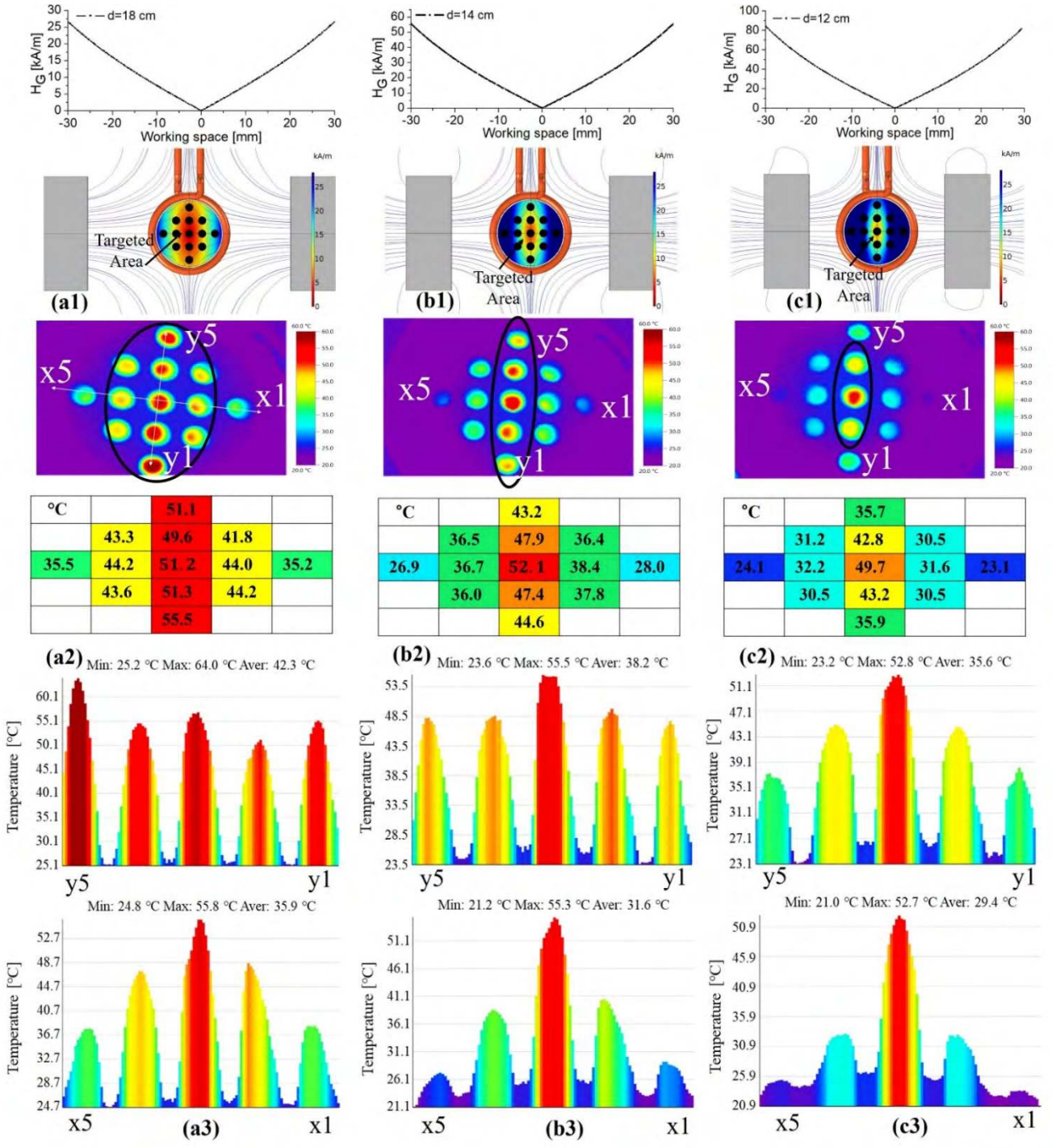

FIGURE 6. Controls of FFR and heat distributions when the distance between two magnets is (a1) 18, (b1) 14, and (c1) 12 cm. Magnetic field distribution at the distance of (a2) 18, (b2) 14, and (c2) 12 cm. Corresponding heat distribution of the MNPs using thermal image camera (a3), (b3), and (c3). Histogram of thermal distribution from the position of x1 to the position of x5 and the position of y1 to the position of y5.

FFR improved with increase in the gradient field. When the distance between the two magnets was 12 cm, the generated gradient of the field was 3.53 mT/mm, and the area of the FFR was 3.78 cm^2, as shown in Fig. 6 (c1) and (c2). Under these conditions, the maximum magnetic field was 86 kA/m at the positions of $\pm$ 30 mm. In particular, the area of FFR became the smallest among the three conditions tested and showed the highest accuracy. The applied magnetic field of 64kA/m corresponded to 56.67% of the saturation point of 9.59-nm-sized MNPs and produced a very low temperature increase of 2.94 K.

Therefore, the maximum field of 86 kA/m completely restricted the heat generation at the point x1, as shown in Fig 6 (c3). The temperatures at x1, x2, and x3 were

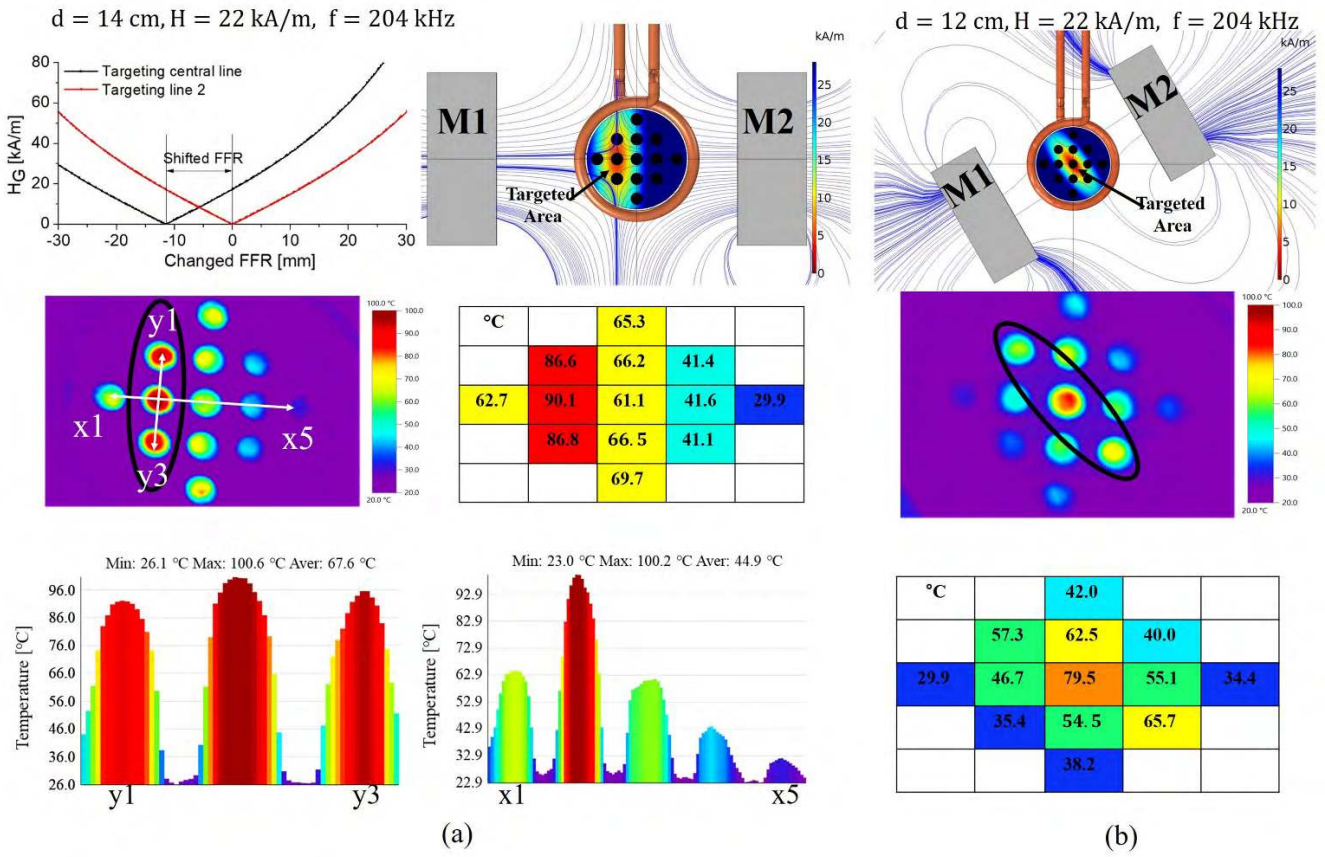

FIGURE 7. **(a) Results of simulation and experiments for translation of FFR: Distribution of field gradient in working space and observation of heat distribution for the changed FFR. (b) Magnetic field distribution for rotation of FFR and results of heat generation with distribution of MNPs.**

24.1, 32.2, and 49.7 °C, respectively. The area of FFR became smaller and was limited from y1 to y3. When we observed temperature distribution in 13 tubes, the center showed the highest temperature of 49.7 °C. In Fig. 6 (c3), we can see that the heat generation was suppressed except for the heat generation at the center because of a stronger gradient field with higher accuracy of the FFR. Figure 7 shows the results of translation and rotation of the FFR. For translation of the FFR, we applied an AMF of 22 kA/m and 204 kHz with a distance of 14 cm between the two magnets. In addition, the distances from M1 to the center and from M2 to the center were 8.2 and 5.3 cm, respectively. Under these conditions, the FFR moved to −11.4 mm from the center of the two magnets and was formed on the y-axis with respect to the point x2. The simulation results obtained for the position of the FFR was consistent with the heat distribution as demonstrated by the thermal imaging results.

In this experiment, because of an increase in the AMF, the temperature at position x2 was 90.1 °C, whereas the temperature increase of MNPs was restricted toward the x5 position because of the stronger gradient field, as shown in Fig. 7 (a). Figure 7 (b) shows the results of rotation of the FFR. For this experiment, the distance between the two magnets was 12 cm at an AMF operating at 22 kA/m and 204 kHz. The two installed magnets were rotated at 45°. Because of this rotation, the FFR rotated. In the simulation, the FFR rotated by 45° and the actual FFR also rotated by 45°. Through thermal imaging, we observed the temperature distribution. Along with the temperature of 79.5 °C at the center, we could observe temperatures of 57.3 and 65.7 °C for the rotation of 45°.

Through various experiments, we verified the selective heat generation and heat control according to changes in the magnetic field gradient. Typically, high-frequency AMF has been applied for magnetic hyperthermia. However, magnetic hyperthermia using MNPs with the AMF has not been able to avoid damage to normal cells. Therefore, the use and control of the FFR for selective hyperthermia would very useful in clinical applications.

To control the dimensions of the FFR and selective heat generation, we investigated the dimensions of FFR for three types MNPs with sizes of 9.56, 15, and 20 nm with changes in the gradient magnetic fields or distances of up to 20 cm between the two magnets, as shown in Table 3. These calculations assumed that the MNPs showed a magnetization of 30% in the magnetization curves (see Fig. 5 (b)). When the distance between the two magnets was 10 cm, the field gradient was 5.55 mT/mm, and the areas of the generated FFR were 7.41, 0.5, and 0.09 cm^2, whereas for a distance of 20 cm, a field gradient of 0.8 mT/mm and targeted areas

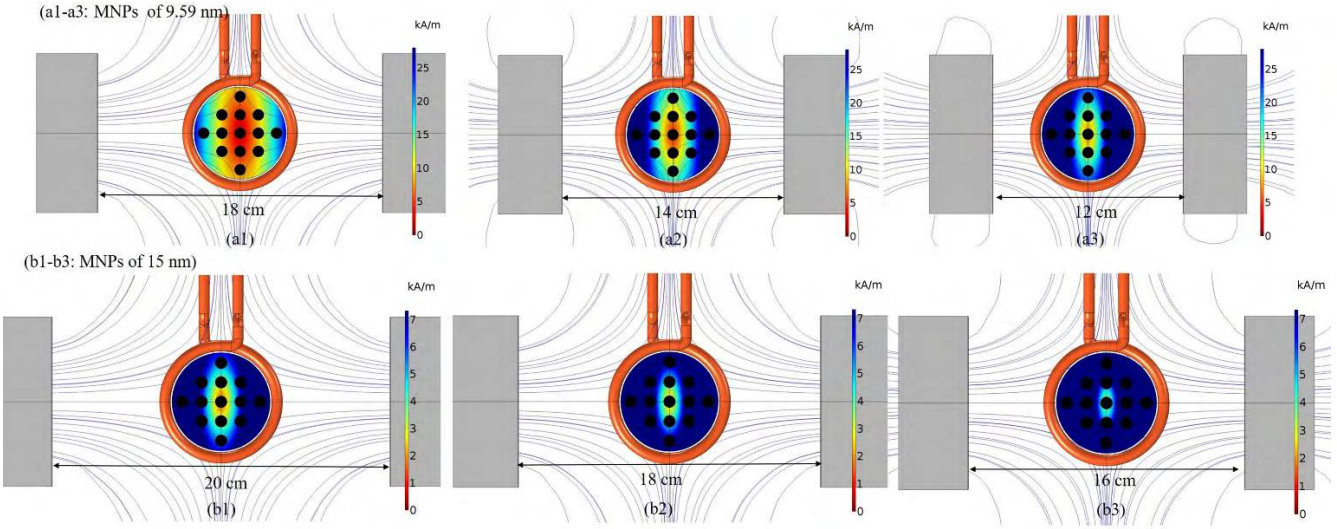

FIGURE 8. Simulation results for variations in the area of FFR according to changes in fiend gradient and the size of MNPs: Magnetic field distributions for FFR in working space using 9.56-nm-sized MNPs at the distance of (a1) 18, (a2) 14, and (a3) 12 cm. When the size of MNPs is 15 nm, variations in FFR at the distance of (b1) 20, (b2) 18, and (b3) 16 cm.

TABLE 3. Relationship between SMF, temperature increase, and Ms %.

Δd (cm)	Targeted Area (cm^{-2})			∇H
	9.59 nm	15nm	20 nm	($mT\ mm^{-1}$)
10	7.41	0.50	0.09	5.55
11	10.40	0.70	0.12	4.41
12	13.25	1.01	0.18	3.53
13	16.09	1.43	0.27	2.85
14	18.94	2.04	0.36	2.33
15	21.17	2.85	0.50	1.92
16	24.16	3.98	0.63	1.59
17	26.03	5.52	0.96	1.33
18	26.24	7.61	1.29	1.11
19	26.24	10.43	1.75	0.94
20	26.24	13.08	2.34	0.80

of 26.24, 13.08, and 2.34 cm^2 were observed for the MNP sizes of 9.59, 15, and 20 nm, respectively. Figure 8 shows the simulation results for the FFR distribution, where a1 to a3 show the magnetic field distribution for the FFR when the MNP size was 9.56 nm and the field gradient was 1.11, 2.33, and 3.53, respectively. In this case, it was confirmed that the generated field distribution for the FFR and the heat distribution of the MNPs were the same. Figure 8 (b1-b3) shows the field distribution for the FFR when we used MNPs with a size of 15 nm at field gradients of 0.8, 1.11, and 1.59 nm, respectively. In this case, the dimensions of FFR were 13.08, 7.61, and 3.98 cm^2, respectively. We were able to confirm the relationship between the size of the MNPs and the distribution of FFR through simulation and experiments. We found that the larger the size of the nanoparticles is, the smaller is the focusing area of the FFR because large MNPs exhibit higher magnetization values than those of small MNPs under the same external magnetic field (see Fig. 5 (b)). However, the narrowed FFR tended not to be completely field-free, as shown in Fig. 8 (b3), because of the relatively strong field gradient.

9.59-nm- and 15-nm-sized MNPs showed different field distributions (dimensions) for the FFR under same field gradient of 1.11 mT/mm, as shown in Fig. 8 (a1) and (b2), respectively. Because of the relatively wide FFR seen for 9.56-nm-sized MNPs, most MNPs showed heat generation, whereas 15-nm-sized MNPs showed relatively narrow FFR characteristics. Most nanoparticles showed limited heat generation and could only generate heat at three locations in the center. So far, studies have reported temperature changes including external static fields for magnetic hyperthermia using AMF and MNPs. In addition, a permanent magnet has been used to generate gradient field and FFR. However, quantitative analysis using permanent magnets for FFR has not been reported so far. Therefore, we conducted magnetic simulations and various experiments to analyze both the generation of FFR and control of heat generation according to changes in the field gradients and the size of MNPs using the two permanent magnets. When a static magnetic field was applied to MNPs shown on the magnetization curve, they reached saturation under a certain static field. At this time, Neel and Brownian motions of MNPs were restricted and heat generation was also restricted. At the saturation point, heat generation does not occur. A uniform magnetic field in the AMF environment of MNPs can limit the temperature increase. However, the FFR cannot occur at a specific position, and all MNPs generate heat. Although temperature characteristics can be controlled, selective heat generation is impossible. When the same poles of two magnets face each other, two gradient magnetic fields are generated from the center of FFR to the magnets. MNPs located in the FFR generate heat due to the influence of the AMF, while MNPs

exposed to gradient magnetic fields can suppress the heat generation. In particular, the strength of the gradient field dependent on the size of MNPs can determine the area of FFR. This is an important factor in determining the accuracy or resolution of selective hyperthermia.

IV. CONCLUSION

Herein, we have proposed a new design and control methods of FFR to achieve selective hyperthermia and temperature control of MNPs used in the process. So far, magnetic hyperthermia suffers from the critical issue of heat generation in normal cells. To overcome this problem, a selective hyperthermia technique using FFR is necessary. A new method for the control of FFR and the conditions for making FFR for selective hyperthermia is thus proposed and verified.

First, we proposed how to determine the strength of the magnetic field for generating the FFR. Second, we determined how the FFR changes with the size of MNPs, magnetization state, and strength of AMF. Third, changes in the temperature of MNPs according to change in the FFR were experimentally analyzed. Finally, it was verified that selective heat generation occurs by controlling the position and area of FFR. Therefore, through this study, we have presented and verified how to determine the design parameter of the system for selective hyperthermia and temperature control of MNPs.

We obtained design parameters for the range of field gradients to control the FFR. Therefore, we were able to select the two permanent magnets required for the purpose. By using larger neodymium magnets, the gradient magnetic field can be increased further, making it possible to target a smaller area. Although increasing the number of magnets can increase the gradient magnetic field in some areas, it is not recommended because it also leads to an increase in the FFR size or to the creation of additional FFRs. Finally, we estimated the distribution of FFR by performing simulations based on the proposed process. The temperature distribution of the MNPs was observed using a thermal imaging camera, and the temperature distribution according to changes in the FFR was confirmed. The permanent magnet to generate the FFR was not controllable because the magnetic field from the magnet is controlled by the distance. Therefore, by using a coil instead of a permanent magnet, the controllability of FFR can be improved. Specification of the coil design can be obtained in the proposed method when replacing from the magnets to the coils.

ACKNOWLEDGMENT

(Armando Ramos Sebastian and Se Hwan Ryu contributed equally to this work.)

REFERENCES

[1] A. E. Deatsch and B. A. Evans, "Heating efficiency in magnetic nanoparticle hyperthermia," *J. Magn. Magn. Mater.*, vol. 354, pp. 163–172, Mar. 2014.

[2] U. Gneveckow, A. Jordan, R. Scholz, V. Brüβ, N. Waldöfner, J. Ricke, A. Feussner, B. Hildebrandt, B. Rau, and P. Wust, "Description and characterization of the novel hyperthermia- and thermoablation-system MFH 300F for clinical magnetic fluid hyperthermia," *Med. Phys.*, vol. 31, no. 6, pp. 1444–1451, Jun. 2004.

[3] M. Johannsen, U. Gneveckow, L. Eckelt, A. Feussner, N. WaldÖFner, R. Scholz, S. Deger, P. Wust, S. A. Loening, and A. Jordan, "Clinical hyperthermia of prostate cancer using magnetic nanoparticles: Presentation of a new interstitial technique," *Int. J. Hyperthermia*, vol. 21, no. 7, pp. 637–647, 2005.

[4] B. Thiesen and A. Jordan, "Clinical applications of magnetic nanoparticles for hyperthermia," *Int. J. Hyperthermia*, vol. 24, no. 6, pp. 467–474, 2008.

[5] B. Kozissnik, A. C. Bohorquez, J. Dobson, and C. Rinaldi, "Magnetic fluid hyperthermia: Advances, challenges, and opportunity," *Int. J. Hyperthermia*, vol. 29, no. 8, pp. 706–714, 2013.

[6] W. J. Atkinson, I. A. Brezovich, and D. P. Chakraborty, "Usable frequencies in hyperthermia with thermal seeds," *IEEE Trans. Biomed. Eng.*, vol. BME-31, no. 1, pp. 70–75, Jan. 1984.

[7] D. Chang, M. Lim, J. A. C. M. Goos, R. Qiao, Y. Y. Ng, F. M. Mansfeld, M. Jackson, T. P. Davis, and M. Kavallaris, "Biologically targeted magnetic hyperthermia: Potential and limitations," *Frontiers Pharmacol.*, vol. 9, P. 831, Aug. 2018.

[8] M. Kettering, H. Richter, F. Wiekhorst, S. Bremer-Streck, L. Trahms, W. A. Kaiser, and I. Hilger, "Minimal-invasive magnetic heating of tumors does not alter intra-tumoral nanoparticle accumulation, allowing for repeated therapy sessions: An *in vivo* study in mice," *Nanotechnol.*, vol. 22, no. 50, Nov. 2011, Art. no. 505102.

[9] O. Veiseh, J. W. Gunn, and M. Zhang, "Design and fabrication of magnetic nanoparticles for targeted drug delivery and imaging," *Adv. Drug Del. Rev.*, vol. 62, no. 3, pp. 284–304, Mar. 2010.

[10] C. He, Y. Hu, L. Yin, C. Tang, and C. Yin, "Effects of particle size and surface charge on cellular uptake and biodistribution of polymeric nanoparticles," *Biomaterials*, vol. 31, no. 13, pp. 3657–3666, May 2010.

[11] I. Khmara, M. Koneracka, M. Kubovcikova, V. Zavisova, I. Antal, K. Csach, P. Kopcansky, I. Vidlickova, L. Csaderova, S. Pastorekova, and M. Zatovicova, "Preparation of poly-L-lysine functionalized magnetic nanoparticles and their influence on viability of cancer cells," *J. Magn. Magn. Mater.*, vol. 427, pp. 114–121, Apr. 2017.

[12] S. E. Krown, D. W. Northfelt, D. Osoba, and J. S. Stewart, "Use of liposomal anthracyclines in Kaposi's sarcoma," *Seminars Oncol.*, vol. 31, pp. 36–52, Sep. 2004.

[13] A. P. Sangnier, S. Preveral, A. Curcio, A. K. A. Silva, C. T. Lefèvre, D. Pignol, Y. Lalatonne, and C. Wilhelm, "Targeted thermal therapy with genetically engineered magnetite magnetosomes@RGD: Photothermia is far more efficient than magnetic hyperthermia," *J. Controlled Release*, vol. 279, pp. 271–281, Jun. 2018.

[14] M. D. Tehrani, J.-H. Yoon, M. O. Kim, and J. Yoon, "A novel scheme for nanoparticle steering in blood vessels using a functionalized magnetic field," *IEEE Trans. Biomed. Eng.*, vol. 62, no. 1, pp. 303–313, Jan. 2015.

[15] A. Priprem, P. Mahakunakorn, C. Thomas, and I. Thomas, "Cytotoxicity studies of superparamagnetic iron oxide nanoparticles in macrophage and liver cells," *Amer. J. Nanotechnol.*, vol. 1, no. 2, pp. 78–85, 2010.

[16] C. Kut, Y. Zhang, M. Hedayati, H. Zhou, C. Cornejo, D. Bordelon, J. Mihalic, M. Wabler, E. Burghardt, C. Gruettner, A. Geyh, C. Brayton, T. L. Deweese, and R. Ivkov, "Preliminary study of injury from heating systemically delivered, nontargeted dextran–superparamagnetic iron oxide nanoparticles in mice," *Nanomedicine*, vol. 7, no. 11, pp. 1697–1711, Nov. 2012.

[17] P. Cantillon-Murphy, L. L. Wald, M. Zahn, and E. Adalsteinsson, "Proposing magnetic nanoparticle hyperthermia in low-field MRI," *Concepts Magn. Reson. A*, vol. 36A, no. 1, pp. 36–47, Feb. 2010.

[18] P. Cantillon-Murphy, L. Wald, E. Adalsteinsson, and M. Zahn, "Heating in the MRI environment due to superparamagnetic fluid suspensions in a rotating magnetic field," *J. Magn. Magn. Mater.*, vol. 322, no. 6, pp. 727–733, Mar. 2010.

[19] K. Murase, H. Takata, Y. Takeuchi, and S. Saito, "Control of the temperature rise in magnetic hyperthermia with use of an external static magnetic field," *Phys. Medica*, vol. 29, no. 6, pp. 624–630, Nov. 2013.

[20] C. P. Gooneratne, A. Kurnicki, S. Yamada, S. C. Mukhopadhyay, and J. Kosel, "Analysis of the distribution of magnetic fluid inside tumors by a giant magnetoresistance probe," *PLoS ONE*, vol. 8, no. 11, Nov. 2013, Art. no. e81227.

[21] B. Gleich and J. Weizenecker, "Tomographic imaging using the nonlinear response of magnetic particles," *Nature*, vol. 435, no. 7046, pp. 1214–1217, Jun. 2005.

[22] J. Weizenecker, B. Gleich, J. Rahmer, H. Dahnke, and J. Borgert, "Three-dimensional real-time *in vivo* magnetic particle imaging," *Phys. Med. Biol.*, vol. 54, no. 5, pp. L1–L10, Feb. 2009.

[23] B. Zheng, M. P. V. See, E. Yu, B. Gunel, K. Lu, T. Vazin, D. V. Schaffer, P. W. Goodwill, and S. M. Conolly, "Quantitative magnetic particle imaging monitors the transplantation, biodistribution, and clearance of stem Cells *In Vivo*," *Theranostics*, vol. 6, no. 3, pp. 291–301, Jan. 2016.
[24] J. Salamon, M. Hofmann, C. Jung, M. G. Kaul, F. Werner, K. Them, R. Reimer, P. Nielsen, A. V. Scheidt, G. Adam, T. Knopp, and H. Ittrich, "Magnetic particle/magnetic resonance imaging: In-vitro MPI-guided real time catheter tracking and 4D angioplasty using a road map and blood pool tracer approach," *PLoS ONE*, vol. 11, no. 6, Jun. 2016, Art. no. e0156899.
[25] T.-A. Le, X. Zhang, A. K. Hoshiar, and J. Yoon, "Real-time two-dimensional magnetic particle imaging for electromagnetic navigation in targeted drug delivery," *Sensors*, vol. 17, no. 9, p. 2050, Sep. 2017.
[26] J. Rahmer, D. Wirtz, C. Bontus, J. Borgert, and B. Gleich, "Interactive magnetic catheter steering with 3-D real-time feedback using multi-color magnetic particle imaging," *IEEE Trans. Med. Imag.*, vol. 36, no. 7, pp. 1449–1456, Jul. 2017.
[27] K. Murase, M. Aoki, N. Banura, K. Nishimoto, A. Mimura, T. Kuboyabu, and I. Yabata, "Usefulness of Magnetic Particle Imaging for Predicting the Therapeutic Effect of Magnetic Hyperthermia," *Open J. Med. Imag.*, vol. 05, no. 2, pp. 85–99, May 2015.
[28] D. Hensley, Z. W. Tay, R. Dhavalikar, B. Zheng, P. Goodwill, C. Rinaldi, and S. Conolly, "Combining magnetic particle imaging and magnetic fluid hyperthermia in a theranostic platform," *Phys. Med. Biol.*, vol. 62, no. 9, pp. 3483–3500, Apr. 2017.
[29] S. L. Ho, S. Niu, and W. N. Fu, "Design and analysis of novel focused hyperthermia devices," *IEEE Trans. Magn.*, vol. 48, no. 11, pp. 3254–3257, Nov. 2012.
[30] T. O. Tasci, I. Vargel, A. Arat, E. Guzel, P. Korkusuz, and E. Atalar, "Focused RF hyperthermia using magnetic fluids," *Med. Phys.*, vol. 36, no. 5, pp. 1906–1912, May 2009.
[31] R. E. Rosensweig, *Ferrohydrodynamics*. Mineola, NY, USA: Dover, 2014.

ARMANDO RAMOS SEBASTIAN received the B.Sc. degree in bionic engineering from the Instituto Politecnico Nacional, Mexico, Mexico, in 2016. He is currently pursuing the M.Eng. degree with the Department of Electronics Convergence Engineering, Wonkwang University, Iksan, South Korea. His current research interests include the design and control of magnetic microrobots for targeted drug delivery, and magnetic hyperthermia.

SE HWAN RYU received the B.S. degree in chemistry from Wonkwang University, in 2018, where he is currently pursuing the M.S. degree under the supervision of Prof. H. M. Ko. His research interests include the development of organic synthesis, catalysis, and organometallic chemistry.

HAYE MIN KO graduated from Kwangwoon University, in 2004, and received the Ph.D. degree in organic chemistry from Seoul National University, under the supervision of Prof. E. Lee. After postdoctoral research with Prof. G. Dong at The University of Texas at Austin, she joined Wonkwang University as an Assistant Professor in 2015, where she has been an Associate Professor in 2018. She has been serving as the Chairman for the Department of Bio-Nano Chemistry, since 2018. Her research interest includes the development and applications of transition metal free reaction.

SUNG HOON KIM (M'12) received the B.S. degree in electronic engineering from Yeungnam University, Gyeongsan, South Korea, in 2005, the M.S. degree in medical and biological engineering from Kyungpook National University, Daegu, South Korea, in 2007, and the Ph.D. degree in electrical communication engineering from Tohoku University, Sendai, Japan, in 2012. He is currently an Associate Professor with the Department of Electronics Convergence Engineering, Wonkwang University, Iksan, South Korea. His research interests include magnetic sensors and actuators, multiscale magnetic micro/nano systems, magnetic hyperthermia, and implantable medical devices.